*Desalination and Water Treatment*
www.deswater.com

doi: 10.5004/dwt.2021.27431

230 (2021) 411–418
August

# Carbon quantum dots decorated $Bi_4O_5I_2$ with greatly improved visible-light photocatalytic performance

Xu Yan[a], Long Pan[a], Yanli Mao[a,*], Haiyan Kang[a], Zhongxian Song[a], Xia Zhang[a], Xiaole Yan[a], Wei Ma[b], Biao Liu[a], Yong Zhao[c,*]

[a]*Henan Province Key Laboratory of Water Pollution Control and Rehabilitation Technology, School of Municipal & Environmental Engineering, Henan University of Urban Construction, Pingdingshan 467000, China, emails: 30020806@hncj.edu.cn (Y.L. Mao), yanxu123987@163.com (X. Yan), 744802812@qq.com (L. Pan), kanghaiyan2007@163.com (H.Y. Kang), songzhongxian@126.com (Z.X. Song), axia6427@163.com (X. Zhang), 420220437@qq.com (X.L. Yan), 30020707@hncj.edu.cn (B. Liu)*
[b]*School of Chemistry and Environmental Engineering, Pingdingshan University, Pingdingshan 467000, China, email: 76219129@qq.com (W. Ma)*
[c]*School of Chemistry and Chemical Engineering, Jiangsu University, Zhenjiang 212013, China, email: zyongujs@163.com (Y. Zhao)*

Received 8 September 2019; Accepted 12 May 2021

**ABSTRACT**

Here we report the construction of carbon quantum dots (CQDs)/$Bi_4O_5I_2$ photocatalyst with improved photocatalytic performance for methyl orange (MO) degradation under visible light. In particular, the CQDs/$Bi_4O_5I_2$ samples synthesized with 2 wt.% CQDs achieved the best performance for the degradation of MO among all samples. This enhancement is ascribed to the optimized CQDs content, which causes the strong light adsorption and efficient electron separation of $Bi_4O_5I_2$. According to the electron spin resonance measurement and quenching experiments, the $^{\bullet}O_2^-$ and $h^+$ were found to be the main active species during the photodegradation process. Moreover, a possible photocatalytic mechanism of CQDs/$Bi_4O_5I_2$ towards MO degradation has been proposed.

*Keywords:* Photocatalyst; Carbon quantum dots; $Bi_4O_5I_2$; Degradation; Visible light

## 1. Introduction

Heterojunction photocatalysts have attracted considerable attention for its potential application in solving energy and environmental crisis [1–4]. In the past few years, many strategies were developed to promote the light absorption, photogenerated charges transfer and separation efficiency of the single photocatalyst, and thus promote the photocatalytic performance [5]. However, the research of visible-light photocatalysts with low-cost, high efficiency, and capable of eliminating environmental pollution is still a hot spot in this field [6,7].

Carbon quantum dots (CQDs), as one of the carbon nanomaterials, have attracted more interest due to their nontoxicity, efficient electron reservoir, and outstanding optical absorption for solar energy conversion [8–11]. Much research is based on the unique electronic properties of CQDs, such as $MoS_2$/CQDs/$ZnIn_2S_4$, CQDs/graphene aerogel, N-CQDs/$SnS_2$, CQDs/$Fe_2O_3$@g-$C_3N_4$, have been devoted to achieving excellent photocatalytic activity for water oxidation or environmental remediation [12–15]. This enhancement is due to the strong electron acceptation of CQDs and excellent photogenerated charge mobility after surface CQDs modification. Recently, 0D/2D photocatalysts has attracted much attention in facilitate the interfacial charge flow and photoinduced carriers separation [16–18]. Therefore, the zero-dimension CQDs can

* Corresponding author.

be an ideal candidate for decorated 2D semiconductor photocatalysts.

$Bi_4O_5I_2$, as one of $I^-$ deficient BiOI, shows superior visible-light adsorption and great potential for application in environmental decontamination [19]. Due to the unique layered structure and self-built internal static electric field, it has large specific surface area and efficient charge carriers' separation, as well as high photocatalytic performance [20–22]. However, the surface charge transfer and separation of $Bi_4O_5I_2$ still need to be optimized, which could further increase the photocatalytic activity of $Bi_4O_5I_2$. For this purpose, many heterojunction photocatalysts were designed to further promoting the charge separation and improving the photocatalytic behavior of $Bi_4O_5I_2$. For example, Sun et al. [23] fabricated BiOI/$Bi_4O_5I_2$ and $Bi_5O_7I$/$Bi_4O_5I_2$ photocatalyst with remarkably improved photocatalytic activity for o-phenyl phenol and 4-tert-butylphenol degradation. Hou et al. [24] designed $Bi_4O_5I_2$/$Bi_2S_3$ heterojunction photocatalyst with improved photocatalytic activity for Cr(VI) reduction. Li et al. [25] synthesized 2D-2D BN/$Bi_4O_5I_2$ composites by ion liquid assisted solvothermal method and explored its visible-light photocatalytic activities for the decomposition of bisphenol A. Jiang et al. [26] demonstrated nitrogen-doped hierarchical carbon (NHC) hybrid with $Bi_4O_5I_2$ as an efficient photocatalyst for methyl orange (MO) degradation under visible light. This has inspired the incorporation of CQDs/$Bi_4O_5I_2$ heterojunction with intimate contacts, efficient interfacial charge separation and high photocatalytic activity.

In this work, CQDs/$Bi_4O_5I_2$ heterojunction photocatalyst was prepared by depositing CQDs on the surface of nanosheets assembled $Bi_4O_5I_2$ nanoflower. The resultant CQDs/$Bi_4O_5I_2$ displayed enhanced photocatalytic performance and good stability for MO degradation under visible light, and the optimal CQDs contents have been identified to be 2 wt.%. The improved photocatalytic activity is due to the enhanced electron–hole separation efficiency. The electron transfer and possible photocatalytic mechanism of CQDs/$Bi_4O_5I_2$ have also been explored.

## 2. Experimental

### 2.1. Preparation of photocatalysts

#### 2.1.1. Synthesis of CQDs

CQDs were obtained according to the procedure of the previous report [27]. Typically, 5.4 mmol citric acid and 335 μL ethylenediamine was added into 10 mL distilled water in a beaker. After sonicated and stirred for 10 min, the mixture was transferred into a 30 mL Teflon-lined autoclave, and heated at 180°C for 5 h. After cooling to room temperature naturally, the obtained product was centrifuged and analyzed by a semipermeable membrane for 12 h. Finally, the purified CQDs solid was gathered by freeze-drying of CQDs solution for 48 h.

#### 2.1.2. Synthesis of $Bi_4O_5I_2$

$Bi_4O_5I_2$ was synthesized obtained using a previously reported procedure [28]: 0.4 mmol $Bi(NO_3)_3{\cdot}5H_2O$ were fully dispersed into 19 mL ethylene glycol by vigorous stirring. Afterwards, 1 mL aqueous solution of 0.4 mmol KI was added dropwise. After that, the suspension was transferred into a 30 mL Teflon-lined autoclave at 130°C for 12 h. The obtained yellow precipitate was collected and washed with water and absolute ethanol and then dried at 60°C for 12 h.

#### 2.1.3. Synthesis of CQDs/$Bi_4O_5I_2$

Typically, 0.1 g $Bi_4O_5I_2$ microspheres were dispersed in 30 mL deionized water and sonicated for 20 min. After mixed with ascertain amount of 1 mg/mL CQDs solution, a brown solution appeared immediately. After stirred and sonicated for 5 min, the mixed solution was transported to a 40 mL Teflon-lined autoclave and heated to 140°C for 4 h. After that, the solid product was collected and dried at 60°C overnight. A series of CQDs/$Bi_4O_5I_2$ photocatalysts were fabricated by adding 0.5, 1, 2 and 3 mL CQDs solution and labeled as 0.5C-$Bi_4O_5I_2$, 1C-$Bi_4O_5I_2$, 2C-$Bi_4O_5I_2$ and 3C-$Bi_4O_5I_2$ (the mass ratios of CQDs to $Bi_4O_5I_2$ were 0.5%, 1%, 2%, and 3%, respectively).

### 2.2. Characterization

X-ray diffraction (XRD) patterns of prepared samples were gathered on a D/Max 2500 diffractometer (Rigaku, Japan) at a scan rate of 10°/min. The scanning electron microscopy images were recorded on an S-4800 field emission scanning electron microscope (Hitachi, Japan). Transmission electron microscopy (TEM) of the images were obtained on JEM-2100 (HR) microscopes. X-ray photoelectron (XPS) spectra were conducted on an ESCALAB 250X electron spectrometer (Thermo, America) with a 150 W Al K$\alpha$ X-ray sources. The UV-Vis diffuse reflectance spectra (DRS) were recorded using an UV-2450 spectrophotometer (Shimadzu, Japan). Fourier-transform infrared (FT-IR) spectra were measured with a Bruker Vertex 70 spectrometer. The photoluminescence (PL) spectra were investigated using a QuantaMaster™ 40 fluorescence spectrofluorometer. The electron spin resonance (ESR) signals of radicals were gathered on a Bruker model JES-FA200 spectrometer. The electrochemical impedance was measured on an electrochemical workstation (CHI-760B, China).

### 2.3. Photocatalytic tests

Photocatalytic activities of fabricated samples were evaluated by photocatalytic degradation of MO under visible light (250 W Xenon lamp with a 420 nm cut-off filter). 50 mg as-prepared photocatalyst was added into 100 mL MO aqueous solution (10 mg/L). After stirring for 30 min in dark to achieve the adsorption-desorption equilibrium, the above mixture solution was sampled (about 5 mL) every 20 min and centrifuged to separate photocatalyst particles for further analysis. The experimental temperature was kept at 25°C by condensed circulating water. The concentration of MO was determined by a UV-Vis spectrophotometer at the wavelength of 464 nm.

### 2.4. Active species investigation

To fully understand the photocatalytic process of MO degradation, series of active species trapping experiments

were conducted. 0.1 mM triethanolamine (TEOA), 1,4-benzoquinone (BQ) and isopropanol (IPA): utilized as the h+, $^{\bullet}O_2^-$, and $^{\bullet}OH$ scavenger, respectively [29]. The method was similar to the former photocatalytic activity test. The electron spin resonance (ESR) signals of $^{\bullet}O_2^-$ and $^{\bullet}OH$ radicals were collected under visible light. 10.0 mg photocatalysts were dispersed in 1 mL methanol or $H_2O$, and then 20 μL DMPO was added as spin-trap reagent, respectively.

## 3. Results and discussion

The phase structures of the as-prepared $Bi_4O_5I_2$ and CQDs/$Bi_4O_5I_2$ samples are firstly measured by XRD, as shown in Fig. 1. The diffraction peaks of as-prepared samples appears at 28.8°, 31.5°, 45.1° and 54.4°, which are correlated to the (–4 –1 1), (4 0 2), (4 2 2), and (811) diffraction planes of $Bi_4O_5I_2$, respectively [30]. Apart from the peaks of $Bi_4O_5I_2$, no other diffraction reflections can be detected, suggesting the high purity of prepared $Bi_4O_5I_2$. After the introduction of CQDs, the characteristic peak of carbon at 26° cannot be observed, which may ascribe to the low concentration of CQDs and the low diffraction intensity in the CQDs/$Bi_4O_5I_2$ samples [31].

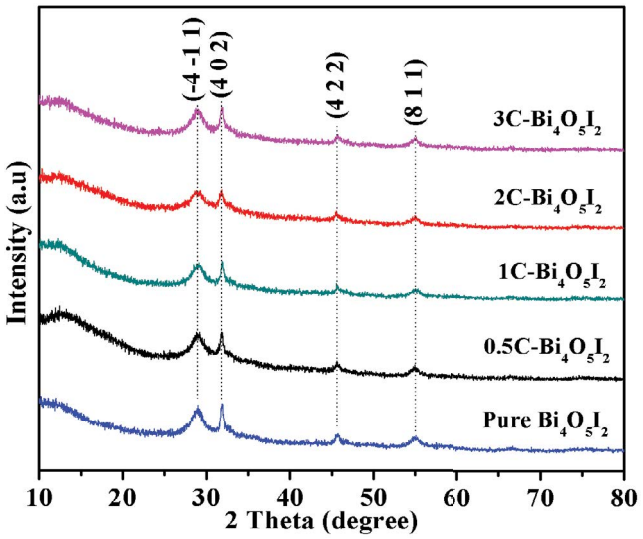


Fig. 1. XRD patterns of $Bi_4O_5I_2$ and CQDs/$Bi_4O_5I_2$ samples.

The morphology and microstructure of the CQDs/$Bi_4O_5I_2$ were studied by field emission scanning electron microscopy (FESEM) and TEM analysis. As can be seen in Fig. 2a, the $Bi_4O_5I_2$ processed microsphere-like (1.5~2 μm), which consisted of many interlaced nanosheets. In Fig. 2b the FESEM image of CQDs/$Bi_4O_5I_2$ remained the similar morphology of pure $Bi_4O_5I_2$, which illustrated the introduction of CQDs did not change the morphology of synthesized samples. As displayed in the TEM image of Fig. 2d, the CQDs are uniformly dispersed with a diameter of about 5 nm. To further confirm the formation of CQDs/$Bi_4O_5I_2$, high-resolution transmission electron microscopy (HRTEM) and high-angle annular dark field-scanning transmission election microscope (HAADF-STEM) utilized to obtain the corresponding element mapping images of the products. The elemental mappings (Fig. 2e) indicate there are only C, Bi, O and I in the samples. HRTEM image of CQDs/$Bi_4O_5I_2$ displays many CQDs are uniformly adhered to the surface of $Bi_4O_5I_2$ nanosheets, which demonstrates that the CQDs have been successfully coupled with $Bi_4O_5I_2$. The interplanar distance of 0.315 nm and 0.335 nm are corresponding to (1 0 0) and (0 0 2) plane of CQDs, respectively. Moreover, the lattice spacing of 0.311, 0.271 and 0.318 nm are corresponding to the (4 1 0), (3 0 3) and (1 1 1) spacing of $Bi_4O_5I_2$. The above results suggest the successful preparation of CQDs/$Bi_4O_5I_2$ photocatalysts.

Furthermore, XPS was carried out to identify the surface chemical composition and status of obtained CQDs/$Bi_4O_5I_2$ photocatalysts. As presented in Fig. 3, two bands at 159.1 and 164.4 eV assigned to the $Bi4f_{5/2}$ and $Bi4f_{7/2}$ [32]. In Fig. 3b, two peaks at 619.2 and 630.7 eV were attributed to $I3d_{5/2}$ and $I3d_{3/2}$, which belong to $I^-$ in $Bi_4O_5I_2$ [33]. In Fig. 3c, two peaks for $O_{1s}$ can be founded at 529.7

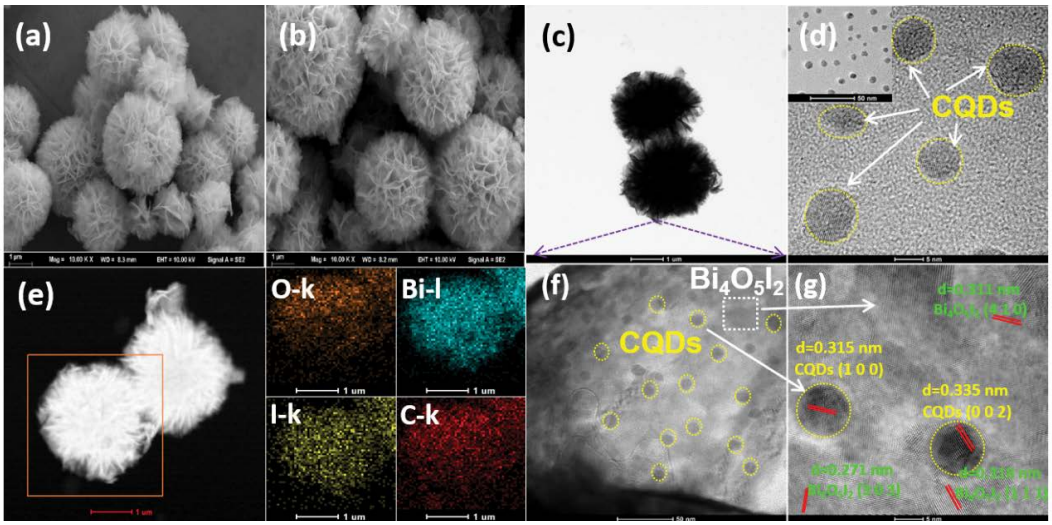


Fig. 2. FESEM images of $Bi_4O_5I_2$ (a) and 2C-$Bi_4O_5I_2$ (b) photocatalysts; TEM images of 2C-$Bi_4O_5I_2$ (c) and CQDs (d). HAADF-STEM image and elemental mappings (e) and HRTEM of the 2C-$Bi_4O_5I_2$.

and 531.4 eV, which ascribed to Bi–O bond in $[Bi_2O_2]^{2+}$ slabs and hydroxyl groups on the surface of $Bi_4O_5I_2$, respectively [34]. Fig. 3d exhibits that the spectrum of C1s could be fitted to three peaks at 284.7, 286.3 and 288.5 eV, which belonged to the C–C, C–O and C=O, respectively [35]. XPS results deduced that the CQDs/$Bi_4O_5I_2$ composite was successfully synthesized.

In Fig. 4, UV-Vis diffuse reflectance spectra (DRS) and optical bandgaps of prepared samples were analyzed to explore the optical property of fabricated samples. As shown in Fig. 4a, the pure $Bi_4O_5I_2$ exhibited the absorption of sunlight shorter than 580 nm. Compared with pure $Bi_4O_5I_2$, CQDs/$Bi_4O_5I_2$ samples showed strong absorption from 500 to 700 nm, suggesting that

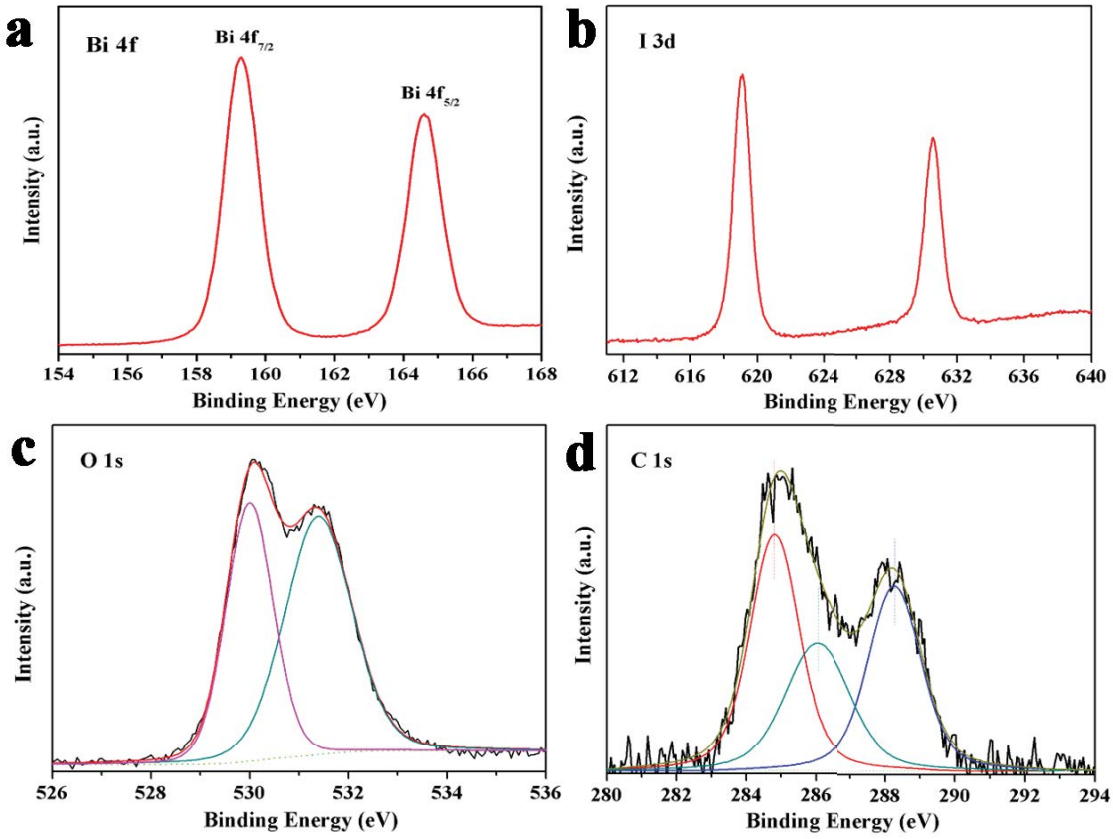


Fig. 3. XPS spectra of 2C-$Bi_4O_5I_2$: (a) Bi 4f spectrum, (b) I 3d spectrum, (c) O 1s spectrum, and (d) C 1s spectrum.

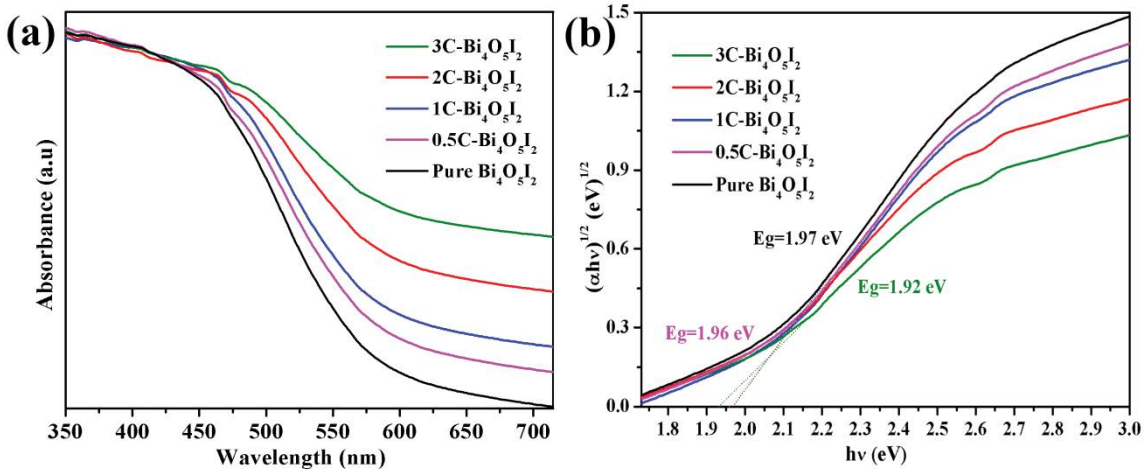


Fig. 4. (a) UV-Vis diffuse reflectance spectra (DRS) of obtained samples and (b) plots of $(\alpha h\nu)^{1/2}$ vs. photon energy ($h\nu$) of pristine $Bi_4O_5I_2$ and CQDs decorated $Bi_4O_5I_2$.

incorporation of the CQDs could enhance the visible light absorption efficiency of $Bi_4O_5I_2$, which is helpful for improving the photoactivity [36]. In Fig. 4b the optical bandgaps of pristine $Bi_4O_5I_2$ and CQDs decorated $Bi_4O_5I_2$ samples are estimated from the Tauc's plot by the following equation:

$$\alpha h\nu = A\left(h\nu - E_g\right)^{n/2} \quad (1)$$

where $\alpha$ is the absorption coefficient, $h$ is Planck's constant, $A$ is a constant, $\nu$ is the light frequency, and $n$ = 1 and 4 for a direct and indirect bandgap materials, respectively. The optical transition of $Bi_4O_5I_2$ is direct and the value of $n$ is thus 1. Therefore, the band gap value of the $Bi_4O_5I_2$ is determined to be 1.97 eV. In order to fully understand the photocatalytic mechanism, the band structure of $Bi_4O_5I_2$ was calculated by the following empirical equation:

$$E_{CB} = X - E^e - 0.5E_g \quad (2)$$

$$E_{VB} = E_{CB} + E_g \quad (3)$$

where $E_{CB}$ and $E_{VB}$ are the conduction band (CB) and valence band (VB) edge potential of sample; $X$ is the absolute electronegativity of the sample (5.93 eV for $Bi_4O_5I_2$); $E_g$ is the bandgap energy of the semiconductor; $E^e$ is the free electrons energy on the hydrogen scale (4.5 eV). Thus, the conduction band and valence band of $Bi_4O_5I_2$ were determined to be +0.445 and +2.415 eV, respectively. The Raman spectra was conducted to explore the structural changes of $Bi_4O_5I_2$ and 2C-$Bi_4O_5I_2$ samples. As presented in Fig. 5, two peaks at 106 and 151 $cm^{-1}$ are assigned to the Bi-I vibration stretching mode of $Bi_4O_5I_2$ [37]. The peaks located at 1300 and 1,517 $cm^{-1}$ are ascribed to the D and G-band of CQDs [38], indicating that 2C-$Bi_4O_5I_2$ was successfully synthesized.

The FT-IR spectra (Fig. 6) also helped determine the surface groups of prepared samples. Compared to the pure $Bi_4O_5I_2$ sample, the peak at 1,387.2 $cm^{-1}$ was assigned to the stretching vibration of the $-COO^-$ groups, revealing the existence of CQD. The peaks at 1,660 and 1,543.6 $cm^{-1}$ belong to the stretching vibration of C=C bonds [39]. The FT-IR results indicate the CQDs/$Bi_4O_5I_2$ have been successfully fabricated. Electrochemical impedance spectroscopy (EIS) was performed to explore the interfacial charge transfer ability of prepared 2C-$Bi_4O_5I_2$ and $Bi_4O_5I_2$ samples. As displayed in Fig. 7, 2C-$Bi_4O_5I_2$ sample possess much smaller diameter of Nyquist circle than that of pure $Bi_4O_5I_2$, indicating the faster interfacial electron transfer of 2C-$Bi_4O_5I_2$ sample. This improvement is attributed to the strong chemical bonding between $Bi_4O_5I_2$ and CQDs.

PL analysis of $Bi_4O_5I_2$ and 2C-$Bi_4O_5I_2$ samples are displayed in Fig. 8. Under the excitation wavelength of 430 nm, the pure $Bi_4O_5I_2$ exhibited sharp emission peaks at ca. 560 nm and two broad shoulder bands at 539 and 578 nm. In the case of 2C-$Bi_4O_5I_2$, the emission peak intensity

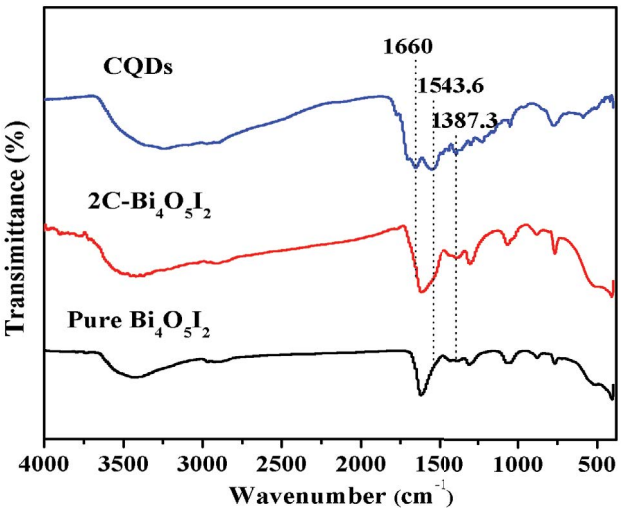


Fig. 6. FT-IR spectra of prepared $Bi_4O_5I_2$, 2C-$Bi_4O_5I_2$ and CQDs samples.

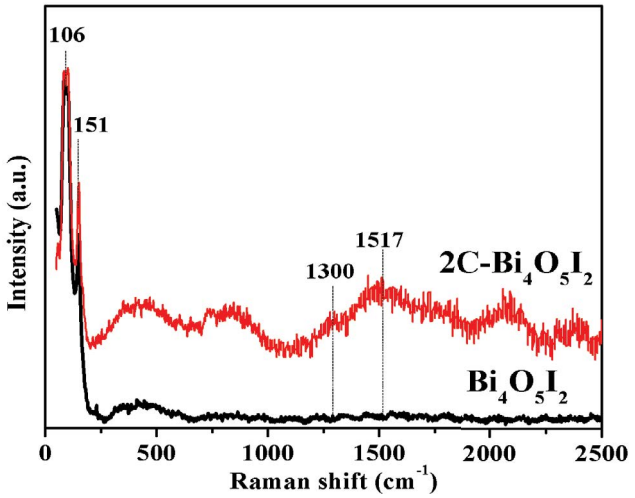


Fig. 5. Raman spectra of $Bi_4O_5I_2$ and 2C-$Bi_4O_5I_2$ samples.

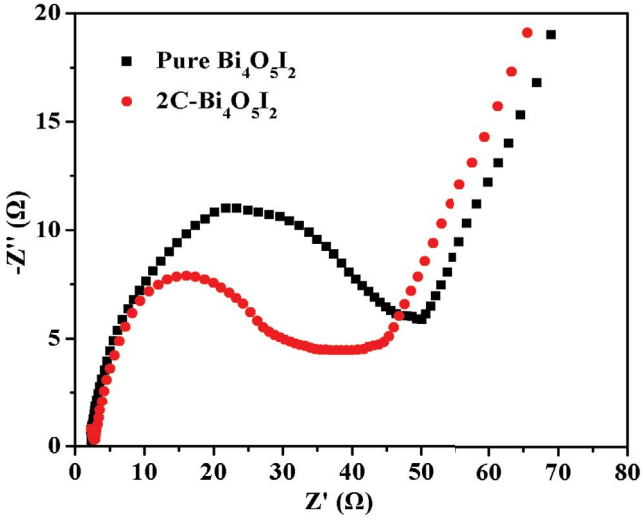


Fig. 7. EIS Nyquist plots of pure $Bi_4O_5I_2$ and 2C-$Bi_4O_5I_2$.

centered at 560 nm is weaker than that of pure $Bi_4O_5I_2$, indicating the increased charge separation efficiency. This improvement is due to the surface loading of CQDs, which can inhibit the high charge recombination of pure $Bi_4O_5I_2$ and promote photocatalytic performance.

In order to evaluate the photocatalytic activity of prepared photocatalysts, MO was chosen as the target contaminant. As shown in Fig. 9a, only 57% MO can be removed by pure $Bi_4O_5I_2$ after 120 min irradiation of visible light. After the introduction of CQDs, the photocatalytic efficiency of CQDs/$Bi_4O_5I_2$ gradually increased, it can be noticed that CQDs/$Bi_4O_5I_2$ prepared with 2 wt.% CQDs (2C-$Bi_4O_5I_2$ sample) display the best photocatalytic efficiency. The removal rate of MO reached 86% after 120 min irradiation, this improvement is due to the excellent visible light absorption capacity of the 2C-$Bi_4O_5I_2$ sample. Fig. 9b shows the photodegradation kinetics of MO over different samples, all the results are fitted by a first-order kinetic model. The 2C-$Bi_4O_5I_2$ sample showed the maximum value of $k$ (0.01479 $min^{-1}$), which was approximately 3 times higher than that of pure $Bi_4O_5I_2$. The ESR technique was employed to measure the main active species during the photocatalytic experiment. Three peaks located at 3495, 3607, 3525 G area scribe to the oxidation of DMPO in the air. In Fig.9c, a six-peak signal of DMPO-$^{\bullet}O_2^-$ was detected when the sample was exposed to visible light, indicating the generation of $^{\bullet}O_2^-$ [40]. However, no signals for DMPO-$^{\bullet}$OH were found under consistent conditions, implying that the $^{\bullet}$OH radicals were not produced in our experiment. The recyclability of the CQDs/$Bi_4O_5I_2$ photocatalyst was tested five consecutives in the oxidation of MO under optimized conditions. As shown in Fig. 9d, the photocatalytic efficiency of MO remained at 82.7%, indicating the high stability and photocatalytic performance of the prepared heterojunction samples.

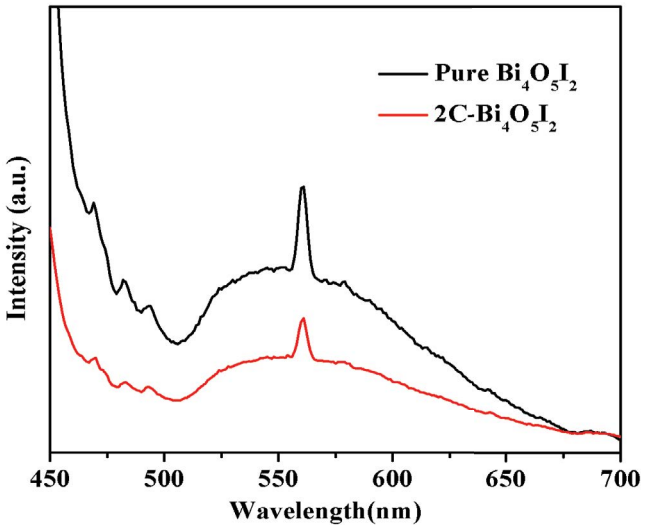


Fig. 8. PL spectra of $Bi_4O_5I_2$and CQDs/$Bi_4O_5I_2$ composite (2C-$Bi_4O_5I_2$) excited at 343 nm.

Based on the above experimental results and analyses, the potential charge separation and MO degradation over CQDs/$Bi_4O_5I_2$ were proposed and illustrated in

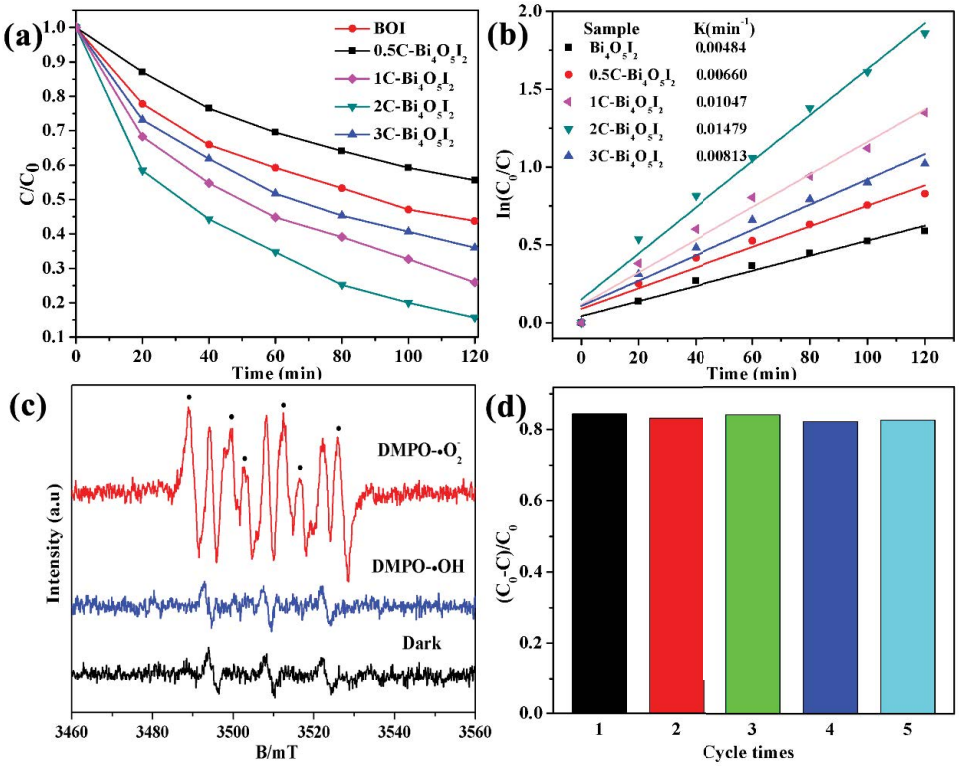


Fig. 9. MO degradation rate (a) and the first-order rate constant (b) of obtained photocatalysts; ESR spectra (c) and cycle experiments (d) of 2C-$Bi_4O_5I_2$ samples under visible light irradiation.

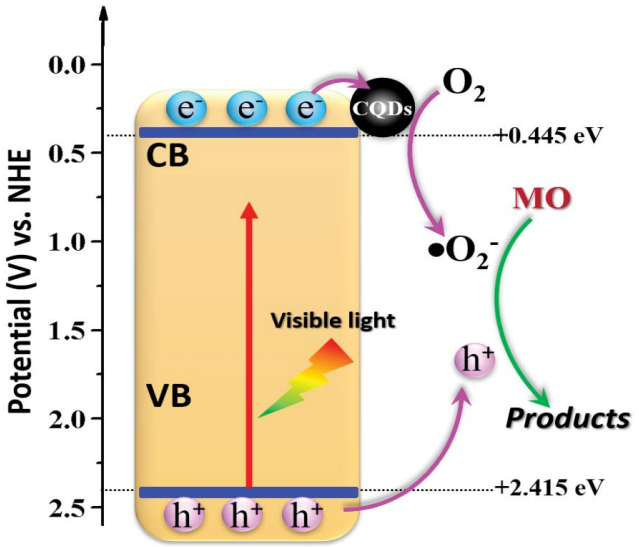


Fig. 10. Schematic illustration for the photocatalytic degradation of MO over CQDs/$Bi_4O_5I_2$ photocatalyst under visible light irradiation.

Fig. 10. The conductive band (CB) of $Bi_4O_5I_2$ is estimated to be +0.445 eV vs. Normal Hydrogen Electrode (NHE) and less negative than that of $O_2/{}^{\bullet}O_2^-$ (–0.33 eV vs. NHE). Thus, electrons in the CB of $Bi_4O_5I_2$ cannot react with $O_2$ to produce ${}^{\bullet}O_2^-$ radical [22]. However, when the CQDs modified on the surface of $Bi_4O_5I_2$, the photogenerated electrons will migrate to the CQDs and react with $O_2$ to produce abundant ${}^{\bullet}O_2^-$ [41]. Additionally, the VB position of $Bi_4O_5I_2$ is too high compared with $OH^-/{}^{\bullet}OH$ (+1.99 V vs. NHE), the holes stored in the VB of $Bi_4O_5I_2$ cannot react with $OH^-$ to produce ${}^{\bullet}OH$ [42]. Therefore, the main reactive species including hole and ${}^{\bullet}O_2^-$, this is consistent with the result of ESR experiments. Here, the CQDs adhered to the surface of $Bi_4O_5I_2$ act as electron acceptors and reservoirs, which lead to enhanced electron transfer and ${}^{\bullet}O_2^-$ production of $Bi_4O_5I_2$, thus, greatly improved the activity for organic degradation.

## 4. Conclusion

In summary, CQDs/$Bi_4O_5I_2$ heterojunction photocatalysts were successfully synthesized with enhanced photocatalytic efficiency for MO degradation compared to pure $Bi_4O_5I_2$under visible light. The introduction of CQDs significantly facilitated the visible light adsorption and photo carriers' separation. The 2C-$Bi_4O_5I_2$ sample displayed excellent photocatalytic activity among all samples. The CQDs/$Bi_4O_5I_2$ heterojunction photocatalysts also showed high stability and reusability. The ${}^{\bullet}O_2^-$ and $h^+$ were confirmed to play the chief role in the photodegradation process. Current work provides a simple and efficient way to improve the photocatalytic activity of $Bi_4O_5I_2$ for contaminants elimination and environment protection.

## Acknowledgments

The authors would like to acknowledge the National Natural Science Foundation of China (U1904174), Key Scientific and Technological Project of Henan Province (2021 02310280, 202102310287, 212102310068), Natural Science Youth Fund of Henan Province (202300410034, 202300410033), Henan Key Scientific Research Projects (20A150009), the Doctoral Research Start-up Project of Henan University of Urban Construction (Q20170094). The authors have declared that no conflict of interest exists.

## References

[1] L. Yang, Y.T. Peng, X.D. Luo, Y. Dan, J.H. Ye, Y. Zhou, Z.G. Zou, Beyond $C_3N_4$ π-conjugated metal-free polymeric semiconductors for photocatalytic chemical transformations, Chem. Soc. Rev., 50 (2021) 2147–2172.
[2] Q. Wang, K. Domen, Particulate photocatalysts for light-driven water splitting: mechanisms, challenges, and design strategies, Chem. Rev., 120 (2020) 919–985.
[3] H.J. Dong, M.Y. Xiao, S.Y. Yu, H.H. Wu, Y. Wang, J.X. Sun, G. Chen, C.M. Li, Insight into the activity and stability of $Rh_xP$ nano-species supported on g-$C_3N_4$ for photocatalytic $H_2$ production, ACS Catal., 10 (2020) 458–462.
[4] Y.G. Chao, P. Zhou, N. Li, J.P. Lai, Y. Yang, Y.L. Zhang, Y.H. Tang, W.X. Yang, Y.P. Du, D. Su, Y.S. Tan, S.J. Guo, Ultrathin visible-light-driven Mo incorporating $In_2O_3$-$ZnIn_2Se_4$ Z-scheme nanosheet photocatalysts, Adv. Mater., 31 (2019) 1807226, doi: 10.1002/adma.201807226.
[5] C.P. Xu, P.R. Anusuyadevi, C. Aymonier, R. Luque, S. Marre, Nanostructured materials for photocatalysis, Chem. Soc. Rev., 48 (2019) 3868–3902.
[6] D.J. Wang, N.B. Saleh, W.J. Sun, C.M. Park, C.Y. Shen, N. Aich, W. Peijnenhurg, W. Zhang, Y. Jin, C.M. Su, Next-generation multifunctional carbon-metal nanohybrids for energy and environmental applications, Environ. Sci. Technol., 53 (2019) 7265–7287.
[7] M.F. Li, Y.G. Liu, G.M. Zeng, N. Liu, S.B. Liu, Graphene and graphene-based nanocomposites used for antibiotics removal in water treatment: a review, Chemosphere, 226 (2019) 360–380.
[8] X. Liu, Y. Yang, H. Li, Z. Yang, Y. Fang, Visible light degradation of tetracycline using oxygen-rich titanium dioxide nanosheets decorated by carbon quantum dots, Chem. Eng. J., 408 (2021) 127259, doi: 10.1016/j.cej.2020.127259.
[9] T. Xian, X.F. Sun, L.J. Di, Y.J. Zhou, J. Ma, H.Q. Li, H. Yang, Carbon quantum dots (CQDs) decorated $Bi_2O_{3-x}$ hybrid photocatalysts with promising NIR-light-driven photodegradation activity for AO7, Catalysts, 9 (2019) 1031, doi: 10.3390/catal9121031.
[10] W.L. Shi, F. Guo, M.Y. Li, Y. Shi, M.F. Wu, Y.B. Tang, Enhanced visible-light-driven photocatalytic $H_2$ evolution on the novel nitrogen-doped carbon dots/$CuBi_2O_4$ microrods composite, J. Alloys Compd., 775 (2019) 511–517.
[11] J.Z. Li, K. Liu, J.L. Xue, G.Q. Xue, X.J. Sheng, H.Q. Wang, P.W. Huo, Y.S. Yan, CQDs preluded carbon-incorporated 3D burger-like hybrid ZnO enhanced visible-light-driven photocatalytic activity and mechanism implication, J. Catal., 369 (2019) 450–461.
[12] B.Q. Wang, Z.R. Deng, X.Z. Fu, Z.H. Li, $MoS_2$/CQDs obtained by photoreduction for assembly of a ternary $MoS_2$/CQDs/$ZnIn_2S_4$ nanocomposite for efficient photocatalytic hydrogen evolution under visible light, J. Mater. Chem. A, 6 (2018) 19735–19742.
[13] R. Wang, K.Q. Lu, F. Zhang, Z.R. Tang, Y.J. Xu, 3D carbon quantum dots/graphene aerogel as a metal-free catalyst for enhanced photosensitization efficiency, Appl. Catal., B, 233 (2018) 11–18.
[14] S. Wang, L.P. Li, Z.H. Zhu, M.L. Zhao, L.M. Zhang, N.N. Zhang, Q.N. Wu, X.Y. Wang, G.S. Li, Remarkable improvement in photocatalytic performance for tannery wastewater processing via $SnS_2$ modified with N-doped carbon quantum dots: synthesis, characterization, and 4-nitrophenol-aided Cr(VI) photoreduction, Small, 15 (2019) 1804515, doi: 10.1002/smll.201804515.
[15] S.S. Yi, J.M. Yan, Q. Jiang, Carbon quantum dot sensitized integrated $Fe_2O_3$@g-$C_3N_4$ core-shell nanoarray photoanode

towards highly efficient water oxidation, J. Mater. Chem. A, 6 (2018) 9839–9845.
[16] W.L. Shi, J.B. Wang, S. Yang, X. Lin, F. Guo, J.Y. Shi, Fabrication of a ternary carbon dots/CoO/g-$C_3N_4$ nanocomposite photocatalyst with enhanced visible-light-driven photocatalytic hydrogen production, J. Chem. Technol. Biotechnol., 95 (2020) 2129–2138.
[17] W.Y. Lei, Y. Mi, R.J. Feng, P. Liu, S. Hu, J.G. Yu, X.F. Liu, J.A. Rodriguez, J.O. Wang, L. Zheng, K. Tang, S.X. Zhu, G. Liu, M.H. Liu, Hybrid 0D-2D black phosphorus quantum dots-graphitic carbon nitride nanosheets for efficient hydrogen evolution, Nano Energy, 50 (2018) 552–561.
[18] D.L. Huang, Z.H. Li, G.M. Zeng, C.Y. Zhou, W.J. Xue, X.M. Gong, X.L. Yan, S. Chen, W.J. Wang, M. Cheng, Megamerger in photocatalytic field: 2D g-$C_3N_4$ nanosheets serve as support of 0D nanomaterials for improving photocatalytic performance, Appl. Catal., B, 240 (2019) 153–173.
[19] G.J. Wu, Y. Zhao, Y.W. Li, H.M. Ma, J.Z. Zhao, pH-dependent synthesis of iodine-deficient bismuth oxyiodide micro-structures: visible-light photocatalytic activity, J. Colloid Interface Sci., 510 (2018) 228–236.
[20] M. Sun, Y.L. Bi, T. Yan, Y.R. Zhang, T.G. Wu, Y. Shao, D. Wei, B. Du, Room-temperature fabrication of bismuth oxybromide/oxyiodide photocatalyst and efficient degradation of phenolic pollutants under visible light, J. Hazard. Mater., 358 (2018) 20–32.
[21] X.F. Liu, X.Y. Xiong, S.P. Ding, Q.Q. Jiang, J.C. Hu, Bi metal-modified $Bi_4O_5I_2$ hierarchical microspheres with oxygen vacancies for improved photocatalytic performance and mechanism insights, Catal. Sci. Technol., 7 (2017) 3580–3590.
[22] X. Yan, Z.Y. Wu, P.P. Yang, Y.L. Mao, B.A. Liu, Y. Zhao, H. Shen, D.L. Wang, In-situ growth of $Bi_2S_3$ nanocrystals on $Bi_4O_3I_2$ nanostructure with excellent photocatalytic performance under visible light, Catal. Commun., 123 (2019) 91–95.
[23] M. Sun, Q.Q. Wei, Y. Shao, B. Du, T. Yan, L.G. Yan, D.Z. Li, Engineering composition-tunable 3D hierarchical bismuth oxyiodides heterojunctions: ionic liquid-assisted fabrication with strong adsorption ability and enhanced photocatalytic properties, Appl. Catal., B, 233 (2018) 250–259.
[24] D.F. Hou, F. Tang, B.B. Ma, M. Deng, X.Q. Qiao, Y.L. Liu, D.S. Li, $Bi_4O_5I_2$ flower/$Bi_2S_3$ nanorod heterojunctions for significantly enhanced photocatalytic performance, CrystEngComm, 21 (2019) 4158–4168.
[25] M.X. Ji, J.X. Xia, J. Di, Y.L. Liu, R. Chen, Z.G. Chen, S. Yin, H.M. Li, Graphene-like boron nitride induced accelerated charge transfer for boosting the photocatalytic behavior of $Bi_4O_5I_2$ towards bisphenol A removal, Chem. Eng. J., 331 (2018) 355–363.
[26] T. Jiang, J. Jin, J.H. Hou, M. Tahir, F. Idrees, $Bi_4O_5I_2$/nitrogen-doped hierarchical carbon (NHC) composites with tremella-like structure for high photocatalytic performance, Chemosphere, 229 (2019) 426–433.
[27] C.Y. Huang, Y.Z. Hong, X. Yan, L.S. Xiao, K. Huang, W. Gu, K.L. Liu, W.D. Shi, Carbon quantum dot decorated hollow $In_2S_3$ microspheres with efficient visible-light-driven photocatalytic activities, RSC Adv., 6 (2016) 40137–40146.
[28] Q.C. Liu, D.K. Ma, Y.Y. Hu, Y.W. Zeng, S.M. Huang, Various bismuth oxyiodide hierarchical architectures: alcohothermal-controlled synthesis, photocatalytic activities, and adsorption capabilities for phosphate in water, ACS Appl. Mater. Interfaces, 5 (2013) 11927–11934.
[29] X. Lin, C. Liu, J. Wang, S. Yang, J. Shi, Y. Hong, Graphitic carbon nitride quantum dots and nitrogen-doped carbon quantum dots co-decorated with $BiVO_4$ microspheres: a ternary heterostructure photocatalyst for water purification, Sep. Purif. Technol., 226 (2019) 117–127.
[30] H.Q. Cheng, J. Wu, F.G. Tian, L.L. Zhao, Z. Ji, F.Q. Li, Q.W. Li, Z.Z. Guan, T.Y. Zhou, In-situ crystallization for fabrication of BiOI/$Bi_4O_5I_2$ heterojunction for enhanced visible-light photocatalytic performance, Mater. Lett., 232 (2018) 191–195.
[31] J. Wang, L. Tang, G. Zeng, Y. Deng, H. Dong, Y. Liu, L. Wang, B. Peng, C. Zhang, F. Chen, 0D/2D interface engineering of carbon quantum dots modified $Bi_2WO_6$ ultrathin nanosheets with enhanced photoactivity for full spectrum light utilization and mechanism insight, Appl. Catal., B, 222 (2018) 115–123.
[32] X. Yuan, J. Zhang, M. Yan, M. Si, L. Jiang, Y. Li, H. Yu, J. Zhang, G. Zeng, Nitrogen doped carbon quantum dots promoted the construction of Z-scheme system with enhanced molecular oxygen activation ability, J. Colloid Interface Sci., 541 (2019) 123–132.
[33] Y.Y. Yang, C.G. Niu, X.J. Wen, L. Zhang, C. Liang, H. Guo, D.L. Guan, H.Y. Liu, G.M. Zeng, Fabrication of visible-light-driven silver iodide modified iodine-deficient bismuth oxyiodides Z-scheme heterojunctions with enhanced photocatalytic activity for Escherichia coli inactivation and tetracycline degradation, J. Colloid Interface Sci., 533 (2019) 636–648.
[34] Y.H. Lee, Y.M. Dai, J.Y. Fu, C.C. Chen, A series of bismuth-oxychloride/bismuth-oxyiodide/graphene-oxide nanocomposites: synthesis, characterization, and photcatalytic activity and mechanism, Mol. Catal., 432 (2017) 196–209.
[35] J. Shen, J.J. Xue, G.Y. He, J. Ni, Z.X. Chen, B. Tang, Z.W. Zhou, H.Q. Chen, Construction of 3D marigold-like $Bi_2WO_6$/$Ag_2O$/CQDs heterostructure with superior visible-light active photocatalytic activity toward tetracycline degradation and selective oxidation, J. Mater. Sci., 53 (2018) 12040–12055.
[36] R.N. Yin, Y. Li, K.D. Zhong, H. Yao, Y.M. Zhang, K.R. Lai, Multifunctional property exploration: $Bi_4O_5I_2$ with high visible light photocatalytic performance and a large nonlinear optical effect, RSC Adv., 9 (2019) 4539–4544.
[37] M.X. Ji, Y.L. Liu, J. Di, R. Chen, Z.G. Chen, J.X. Xia, H.M. Li, N-CQDs accelerating surface charge transfer of $Bi_4O_5I_2$ hollow nanotubes with broad spectrum photocatalytic activity, Appl. Catal., B, 237 (2018) 1033–1043.
[38] S.P. Ratnayake, M. Mantilaka, C. Sandaruwan, D. Dahanayake, E. Murugan, S. Kumar, G.A.J. Arnaratunga, K.M.N. de Silva, Carbon quantum dots-decorated nano-zirconia: a highly efficient photocatalyst, Appl. Catal., A, 570 (2019) 23–30.
[39] T. Kulandaivalu, S.A. Rashid, N. Sabli, T.L. Tan, Visible light assisted photocatalytic reduction of $CO_2$ to ethane using CQDs/$Cu_2O$ nanocomposite photocatalyst, Diamond Relat. Mater., 91 (2019) 64–73.
[40] H.J. He, L.H. Huang, Z.J. Zhong, S.Z. Tan, Constructing three-dimensional porous graphene-carbon quantum dots/g-$C_3N_4$ nanosheet aerogel metal-free photocatalyst with enhanced photocatalytic activity, Appl. Surf. Sci., 441 (2018) 285–294.
[41] S.K. Le, W.J. Li, Y.J. Wang, X. Jiang, X.X. Yang, X.J. Wang, Carbon dots sensitized 2D-2D heterojunction of $BiVO_4$/$Bi_3TaO_7$ for visible light photocatalytic removal towards the broad-spectrum antibiotics, J. Hazard. Mater., 376 (2019) 1–11.
[42] H.J. Gao, C.X. Zheng, H. Yang, X.W. Niu, S.F. Wang, Construction of a CQDs/$Ag_3PO_4$/$BiPO_4$ heterostructure photocatalyst with enhanced photocatalytic degradation of rhodamine B under simulated solar irradiation, Micromachines, 10 (2019) 557, doi: 10.3390/mi10090557.